Boosting oxygen evolution over inverse spinel Fe-Co-Mn oxide nanocubes through electronic structure engineering

Document license:
TAVERNE

DOI:
[10.1016/j.cej.2021.134446](10.1016/j.cej.2021.134446)

Document status and date:
Published: 01/04/2022

Document Version:
Publisher's PDF, also known as Version of Record (includes final page, issue and volume numbers)

Please check the document version of this publication:

• A submitted manuscript is the version of the article upon submission and before peer-review. There can be important differences between the submitted version and the official published version of record. People interested in the research are advised to contact the author for the final version of the publication, or visit the DOI to the publisher's website.
• The final author version and the galley proof are versions of the publication after peer review.
• The final published version features the final layout of the paper including the volume, issue and page numbers.

Link to publication

Boosting oxygen evolution over inverse spinel Fe-Co-Mn oxide nanocubes through electronic structure engineering

Zhuang Zeng [a,1], Siyu Kuang [a,1], Zhen-Feng Huang [a], Xiaoyi Chen [a], Yaqiong Su [b,d,*], Yue Wang [a,c,*], Sheng Zhang [a,c,*], Xinbin Ma [a,c]

[a] *Key Laboratory for Green Chemical Technology of Ministry of Education, Collaborative Innovation Centre of Chemical Science and Engineering, School of Chemical Engineering and Technology, Tianjin University, Tianjin 300072, PR China*
[b] *School of Chemistry, Xi'an Key Laboratory of Sustainable Energy Materials Chemistry, State Key Laboratory of Electrical Insulation and Power Equipment, Xi'an Jiaotong University, Xi'an 710049, PR China*
[c] *Joint School of National University of Singapore and Tianjin University, International Campus of Tianjin University, Binhai New City, Fuzhou 350207, PR China*
[d] *Laboratory of Inorganic Materials and Catalysis, Department of Chemical Engineering and Chemistry, Eindhoven University of Technology, P.O. Box 513, 5600 MB Eindhoven, the Netherlands*

ARTICLE INFO

ABSTRACT

Fossil fuels are urgent to be replaced with renewable energies to achieve carbon neutrality. Intermittent renewable energies such as solar and wind could be stored in chemical bonds, such as hydrogen and carbon-containing chemicals through water and CO_2 electrolyzers respectively. Those two energy systems share a common anodic reaction, the sluggish oxygen evolution reaction (OER), which currently relies on precious noble metals to achieve a reasonable energy conversion efficiency. Herein, tuning the *d*-band center of Fe-based inverse spinel oxides has been achieved through compositions and morphologies engineering. Ternary $Mn_{0.5}Co_{0.5}Fe_2O_4$ nanocubes exhibit oxygen evolution activity superior to the benchmark RuO_2. Mössbauer and in-situ infrared spectra combined with density functional theory calculations prove that the optimized *d*-band center offers a balanced adsorption strength of intermediate *OOH on $Mn_{0.5}Co_{0.5}Fe_2O_4$ nanocubes. This work provides a promising approach to the design and synthesis of highly efficient electrocatalysts beyond oxygen evolution.

1. Introduction

Renewable energy technologies such as solar and wind are important solutions to current environmental problems and energy crisis. However, their inconsistent output prevents them from becoming mainstream in the electricity supply at the moment. The conversion of unstable electricity output to hydrogen through water electrolyzers is one promising renewable energy solution [1–4]. Hydrogen is an ideal alternative energy source for achieving carbon neutrality due to its high energy density, emission-free combustion, and abundant sources [5–8]. The electrolytic water splitting consists of hydrogen evolution reaction (HER) and oxygen evolution reaction (OER), in which the HER reaction is a two-electron process with fewer intermediates, less energy barrier, and higher efficiency. However, the OER is a four-electron process that involves multiple reaction pathways and intermediates, high energy barrier made it kinetically slower. Therefore, the OER is the key process

that determines the overall efficiency of electrochemical water splitting [9–14]. In addition, OER is often coupled with other energy systems, such as CO_2 electrolyzers converting CO_2 into carbon containing chemicals and fuels [15,16]. Thus, it is imperative to develop high-performance electrocatalysts that can effectively reduce the kinetic limitation of OER and improve the efficiency of water splitting [17–20].

Noble metal-based catalysts, such as IrO_x and RuO_x are generally considered to be the state-of-the-art OER electrocatalysts [21–24], but their high price and limited reserves seriously hinder their large-scale industrial applications [25–27]. Therefore, 3d transition metal oxides, such as Fe, Co, Ni, and Mn oxides have been extensively studied for their OER activities [28–32]. Especially, transition metal spinel oxides (AB_2O_4), where A^{x+} and B^{x+} cations occupy the tetrahedral and octahedral sites, respectively, have attracted substantial attention due to their abundance and low cost [31,33–35]. Tremendous efforts have been spent improving OER activity of spinel oxides. Among them,

---

* Corresponding authors.
E-mail addresses: yqsu1989@xjtu.edu.cn (Y. Su), yuewang@tju.edu.cn (Y. Wang), sheng.zhang@tju.edu.cn (S. Zhang).
[1] These authors contributed equally to this work.

incorporating heterometal atoms into the octahedral sites or tetrahedral sites of the spinel has been proven to be an effective strategy to enhance its OER activity, where the intermediate adsorption energy is optimized through tailoring the *d*-band center [36]. Duan et al. [35] introduced Ni into the octahedral sites of $ZnCo_2O_4$ spinel oxide and found that the lattice oxygen in the metastable $ZnCo_{1.2}Ni_{0.8}O_4$ facilitated the oxy-hydroxide formation and subsequent oxygen evolution process. In addition, Sun et al. [31] demonstrated that the OER activity of spinel oxides was related to the covalency competition between the metal cations in tetrahedral and octahedral sites, and found that $[Mn]_T[Al_{0.5}Mn_{1.5}]_OO_4$ showed superior OER activity. Recently, Lu et al. [37] reported that the cationic intercalation with Fe^{3+} resulted in the conversion of stable Mn^{4+} (d^3 state) to high-spin Mn^{3+} (d^4 state), which improves the adsorption ability for free –OH and enhances the OER activity. Although significant improvement has been reached, the strategies to enhance OER activity through electronic structure engineering are still needed to explore. And it is still challenging to develop efficient electrocatalysts with superior OER activity than that of the benchmark RuO_2 catalyst. Thus, it is essential to tune the structures and components to further boost their OER activity.

In the active catalytic center (Mn_4CaO_5) for oxygen evolution in natural photosynthesis [38,39], Mn is the key element and found to be more suitable for the formation of O-O bond than other transition metal elements [40]. In addition, the various chemical and structural properties of Mn-based and Co-based materials provide numerous degrees of freedom to design high-performance water splitting catalysts [40]. Herein, we reported a synthetic strategy for doping Co or Mn into inverse spinel Fe oxides with different exposed facets. Among those samples, ternary cubic inverse spinel $Mn_{0.5}Co_{0.5}Fe_2O_4$ exposed with (400) facets showed the highest OER activity and better than the benchmark RuO_2. This enhanced OER activity was attributed to the synergistic facet and composition effect, which optimizes the bond strength between cubic $Mn_{0.5}Co_{0.5}Fe_2O_4$ surface and intermediates, and thus reduces the energy barrier of the potential-limiting step (PLS) as manifested by detailed electrochemical and density functional theory (DFT) simulation. In-situ ATR-IR has been carried out to detect the key intermediate (OOH*) to indicate the OER mechanism is mainly the adsorbate evolution mechanism (AEM).

2. Results and discussions

2.1. *$Co_xFe_{3-x}O_4$ binary catalysts*

Monometallic Fe_3O_4 and Co_3O_4 nanoparticles, and bimetallic $Co_xFe_{3-x}O_4$, as well as trimetallic $Mn_xCo_{1-x}Fe_2O_4$ have been successfully synthesized through a thermal decomposition of metal (Fe, Co, Mn)-oleate complex using 1-octadecene as the solvent and oleic acid as the reducing agent and stabilizer, respectively (Scheme 1). Intriguingly, the morphology of the nanoparticles could be modulated facilely to be cubic or spherical by washing the obtained metal oleate complex with H_2O thoroughly or not. In brief, cubic nanoparticles could be obtained directly via a thermal decomposition process without washing the oleate complex so that a few residual Na-oleate might exist and it led to the formation of cubic NPs preferentially [41]. In contrast, spherical

morphology was obtained if washing the metal oleate complex with water thoroughly so that oleic acid (OA) would play a dominant role in the crystal nucleation and growth which led to the spherical morphology.

Monometallic Fe_3O_4 and Co_3O_4, and bimetallic $Co_xFe_{3-x}O_4$ (x = 0.75 and 1) nanoparticles were successfully prepared with uniform particle size distributions. Transmission electron microscope (TEM) of the cubic $CoFe_2O_4$ NPs in **Figure S1a** exhibited a nearly uniform cubic morphology with a mean size of ca. 10 nm. High-resolution transmission electron microscope (HRTEM) image (**Figure S1b**) showed the dominant (400) plane with an interplanar spacing of 2.19–2.20 Å. Furthermore, the selected area electron diffraction (SAED) image (**Figure S1c**) also manifested the (400) facet was dominant with the brightest ring. TEM image (**Figure S1d**) of supported $CoFe_2O_4$ catalyst indicated that the cubic nanoparticles dispersed uniformly on carbon support. Scanning transmission electron microscope- X-ray energy dispersive spectroscopy (STEM-EDS) element mappings (**Figure S1e-i**) demonstrated the uniform locations of Co, Fe, and O elements in the spinel nanoparticles. The electron microscopic characterizations for monometallic Fe_3O_4 and Co_3O_4, as well as bimetallic $Co_{0.75}Fe_{2.25}O_4$ nanoparticles before and after loading in carbon were shown in **Figure S2**, both of them showed an approximately cubic morphology with an average particle size of ca. 10 nm, which was similar to that of $CoFe_2O_4$.

We then evaluated OER activities of bimetallic $Co_{0.75}Fe_{2.25}O_4$ and $CoFe_2O_4$, as well as monometallic Fe_3O_4 and Co_3O_4 catalysts. The OER polarization curves and the current density at a given potential of 1.6 V of the cubic Co-Fe catalysts and commercial RuO_2 catalyst in O_2-saturated 1.0 M KOH with a rotating disk electrode (RDE) were shown in the **Figure S3a and Figure S3b**. Bimetallic $Co_xFe_{3-x}O_4$ catalysts exhibited a higher OER activity ($Co_{0.75}Fe_{2.25}O_4$: 7.4 mA cm^{-2} and $CoFe_2O_4$:10.2 mA cm^{-2}) than that of monometallic Fe_3O_4 (2.7 mA cm^{-2}) and Co_3O_4 (1.82 mA cm^{-2}), but lower than benchmark RuO_2 (22.3 mA cm^{-2}). The overpotentials at a current density of 10 mA cm^{-2} and the Tafel slopes were also calculated, as shown in **Figure S3c** and **Figure S3d**, bimetallic $Co_xFe_{3-x}O_4$ catalysts showed lower overpotentials and Tafel slope than monometallic Fe or Co-based catalysts, indicating a better OER activities, but it's still not as good as commercial RuO_2 catalysts.

2.2. *$Mn_xCo_{1-x}Fe_2O_4$ ternary catalysts*

Inspired by the fact that Mn-containing complex (Mn_4CaO_5) serves as the catalytic activity center for oxygen evolution in natural photosynthesis [38,40], we further incorporated Mn into the CoFe bimetallic catalysts and fabricated the ternary $Mn_xCo_{1-x}Fe_2O_4$ catalysts to boost the OER activity. Typical TEM images of $Mn_{0.5}Co_{0.5}Fe_2O_4$ in Fig. 1a showed that a nearly monodisperse nanocubes with particle size of ca. 10 nm were obtained. HRTEM image in Fig. 1b showed two groups of definite lattice fringes with the interplanar spacing of 2.25 Å and 1.59 Å and an angle of 45 °, corresponding to the (400) and (440) planes in inverse spinel $Mn_{0.5}Co_{0.5}Fe_2O_4$. Moreover, SAED image in Fig. 1c indicated the polycrystalline nature of the cubic $Mn_{0.5}Co_{0.5}Fe_2O_4$ NPs with two clear bright rings, which are attributed to (400) and (440) planes of the inverse spinel oxide, which is consistent with the HRTEM results in Fig. 1b. STEM image (Fig. 1d) of supported $Mn_{0.5}Co_{0.5}Fe_2O_4$ /C catalyst showed that the cubic nanoparticles are dispersed uniformly on the carbon support, which is beneficial for OER. STEM-EDS element mappings demonstrated that Mn, Co, Fe, O were uniformly distributed in the spinel nanoparticles (Fig. 1e-i).

In addition, another two $Mn_xCo_{1-x}Fe_2O_4$ catalysts with different Mn/Co molar ratio, denoted as $Mn_{0.2}Co_{0.8}Fe_2O_4$ and $Mn_{0.8}Co_{0.2}Fe_2O_4$ were also prepared. As shown in **Figure S4a** and **Figure S4d**, these two catalysts also appeared to be perfectly cubic morphology, and their mean particle sizes were all approximately 10 nm, close to that of $Mn_{0.5}Co_{0.5}Fe_2O_4$. Moreover, the facets of (400) and (440) were still dominant (**Figure S4b** and **Figure S4e**).

X-ray diffraction (XRD) patterns of the ternary MnCoFe catalysts
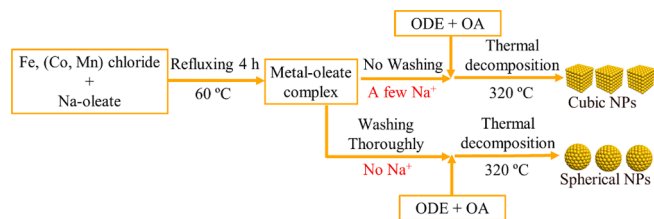
Scheme 1. Schematic illustration of the fabrication of cubic and spherical inverse spinel nanoparticles.
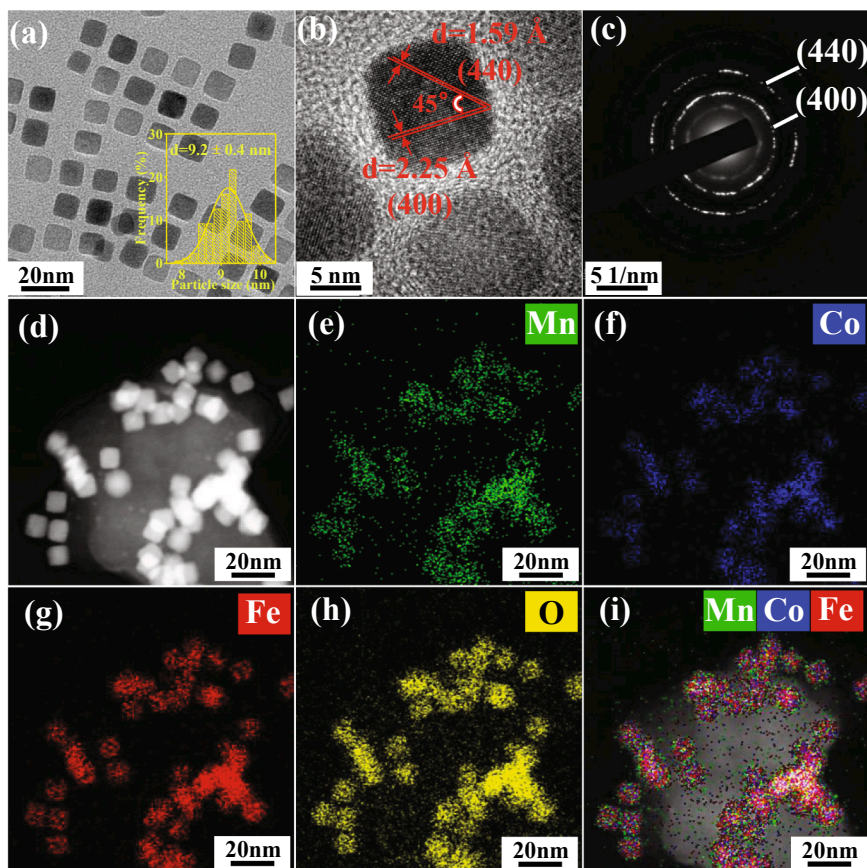
Fig. 1. (a) TEM image and particle size distribution (PSD) histogram (the inset), (b) HRTEM image, and (c) SAED pattern of cubic $Mn_{0.5}Co_{0.5}Fe_2O_4$ nanoparticles, (d-i) STEM image and the corresponding EDS elemental (Mn, Co, Fe, O) mappings of supported $Mn_{0.5}Co_{0.5}Fe_2O_4$ /C catalyst.

were shown in Fig. 2a, the diffraction peaks at $2\theta \approx 35.4\degree$, $43.1\degree$ and $62.6\degree$ could be attributed to the (311), (400) and (440) planes in inverse spinel $Mn_xCo_{1-x}Fe_2O_4$ (PDF: 22–1086). Furthermore, the intensity ratios of (400) to (311) facets (I_{400}/I_{311}) were calculated to be between 4.6 and 5.1 in these three catalysts, which were an order of magnitude higher than the I_{400}/I_{311} ratio of 0.2 in a standard card of PDF: 22–1086. The preferred exposure of (400) and (440) facets originated from the unique cubic structure. This is consistent with the previous research in

which the Fe_3O_4 nanocubes showed enhanced (400) and (440) reflections due to the alignment of their $\langle 100 \rangle$ axis perpendicular to the substrate [41]. And it is noteworthy that the diffraction peaks of (400) and (311) gradually shifted to a lower angle with the increase of Mn/Co ratio, suggesting the slight expansion of the crystal lattice of $Mn_xCo_{1-x}Fe_2O_4$ due to the larger atomic radius of Mn than Co.

X-ray photoelectron spectroscopy (XPS) was used to examine the surface species in the ternary $Mn_xCo_{1-x}Fe_2O_4$ catalysts. The survey scan
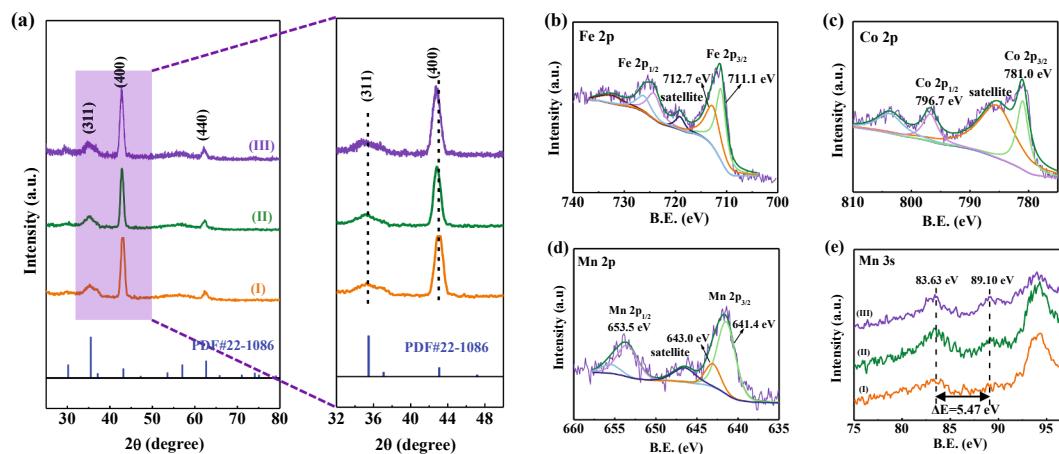

Fig. 2. (a) The XRD patterns of (I) cubic $Mn_{0.2}Co_{0.8}Fe_2O_4$, (II) cubic $Mn_{0.5}Co_{0.5}Fe_2O_4$ and (III) cubic $Mn_{0.8}Co_{0.2}Fe_2O_4$ nanoparticles. The nanoparticles dispersed with hexane were deposited on a Silicon substrate and dried under ambient temperature. (b-d) High-resolution spectra of Fe 2p, Co 2p and Mn 2p of cubic $Mn_{0.5}Co_{0.5}Fe_2O_4$. (e) High-resolution spectra of Mn 3 s of (I) cubic $Mn_{0.2}Co_{0.8}Fe_2O_4$, (II) cubic $Mn_{0.5}Co_{0.5}Fe_2O_4$, (III) cubic $Mn_{0.8}Co_{0.2}Fe_2O_4$.

XPS spectra in **Figure S5** indicated that Mn, Co, Fe, C, and O are the primary surface elements in $Mn_{0.5}Co_{0.5}Fe_2O_4$ catalyst. The surface Mn: Co: Fe atomic ratio is about 0.5: 0.5: 2, which is consistent with the bulk composition detected by ICP-OES and EDS (**Table S1**), indicating a good homogeneity. According to the high-resolution XPS spectra of Fe 2p spectra (**Fig. 2**b), the Fe species was mainly Fe^{3+} cations. Furthermore, the peaks at 711.1 eV and 712.7 eV of Fe $2p_{3/2}$ might correspond to the Fe^{3+} in the tetrahedron and octahedron, respectively [42]. As shown in Fig. 2c, the Co $2p_{3/2}$ peaks centered at 781.0 eV and the Co $2p_{1/2}$ peak at 796.7 eV as well as the shake-up satellites centered at 785.2 eV (Co $2p_{3/2}$) and 803.1 eV (Co $2p_{1/2}$) are attributed to Co^{2+} species [43]. In addition, Mn $2p_{3/2}$ XPS spectra in Fig. 2d show two peaks with binding energy of 643.0 eV and 641.4 eV, which are corresponding to the Mn^{3+} and Mn^{2+} species [44]. The Mn 3s XPS peak was further applied to determine the oxidation states of Mn species. As shown in Fig. 2e, for all the $Mn_xCo_{1-x}Fe_2O_4$ samples, the distance between the two peaks of Mn 3s was ca. 5.47 eV, which also indicates the averaged valence state of Mn is +2.72 [44]. The relative atomic ratio of Fe/Co/Mn in bimetallic and trimetallic catalysts was also determined by ICP-OES and EDS (**Table S1**). The actual metallic atomic ratios were consistent with the molecular formula in each sample.

OER activities of cubic $Mn_xCo_{1-x}Fe_2O_4$ ($Mn_{0.2}Co_{0.8}Fe_2O_4$, $Mn_{0.5}Co_{0.5}Fe_2O_4$, and $Mn_{0.8}Co_{0.2}Fe_2O_4$) and the benchmark RuO_2 catalysts in O_2-saturated 1.0 M KOH with a rotating disk electrode (RDE) were shown in Fig. 3a. At a given potential of 1.6 V, $Mn_{0.5}Co_{0.5}Fe_2O_4$

exhibited much higher current density (34.9 mA cm^{-2}) than $Mn_{0.2}Co_{0.8}Fe_2O_4$ (15.3 mA cm^{-2}) and $Mn_{0.8}Co_{0.2}Fe_2O_4$ (9.2 mA cm^{-2}), and even higher than RuO_2 (22.3 mA cm^{-2}). As shown in Fig. 3b, $Mn_{0.5}Co_{0.5}Fe_2O_4$ showed the lowest overpotential of 308 mV at 10 mA cm^{-2}, it is smaller than those of $Mn_{0.2}Co_{0.8}Fe_2O_4$ (347 mV) and $Mn_{0.8}Co_{0.2}Fe_2O_4$ (375 mV), and even lower than that of commercial RuO_2 (325 mV). This performance indicates that the $Mn_{0.5}Co_{0.5}Fe_2O_4$/C is a highly active OER catalyst. As observed in Fig. 3c, the $Mn_{0.5}Co_{0.5}Fe_2O_4$ exhibited the smallest Tafel slope (76.4 mV dec^{-1}), demonstrating the excellent OER kinetics of $Mn_{0.5}Co_{0.5}Fe_2O_4$. Since the carbon black alone possesses a very poor OER activity (**Figure S6**), the excellent OER activity obtained from $Mn_{0.5}Co_{0.5}Fe_2O_4$/C should be attributed to the cubic $Mn_{0.5}Co_{0.5}Fe_2O_4$ nanoparticles.

The stability of the $Mn_xCo_{1-x}Fe_2O_4$ catalysts (ca. 10 nm) with different Mn/Co molar ratios were evaluated by chronoamperometry as shown in Fig. 3d. It is noteworthy that the ternary $Mn_xCo_{1-x}Fe_2O_4$ catalysts (ca. 10 nm) all exhibited a much more excellent stability than commercial RuO_2 catalyst. For example, continuous evaluation of the OER for ca. 20 h at 1.54 V on $Mn_{0.5}Co_{0.5}Fe_2O_4$ catalyst (mean particle size of 9.2 nm) caused a negligible decrease (only 2.84 %) in current density. The outstanding durability of $Mn_{0.5}Co_{0.5}Fe_2O_4$ catalyst might be ascribed to the stable cubic morphology and the interactions between Mn, Co, and Fe in the inverse spinel structure. The cubic morphology of $Mn_{0.5}Co_{0.5}Fe_2O_4$ catalyst was maintained even though after the 20 h durability test (as shown in **Figure S7**), and the particle size was nearly
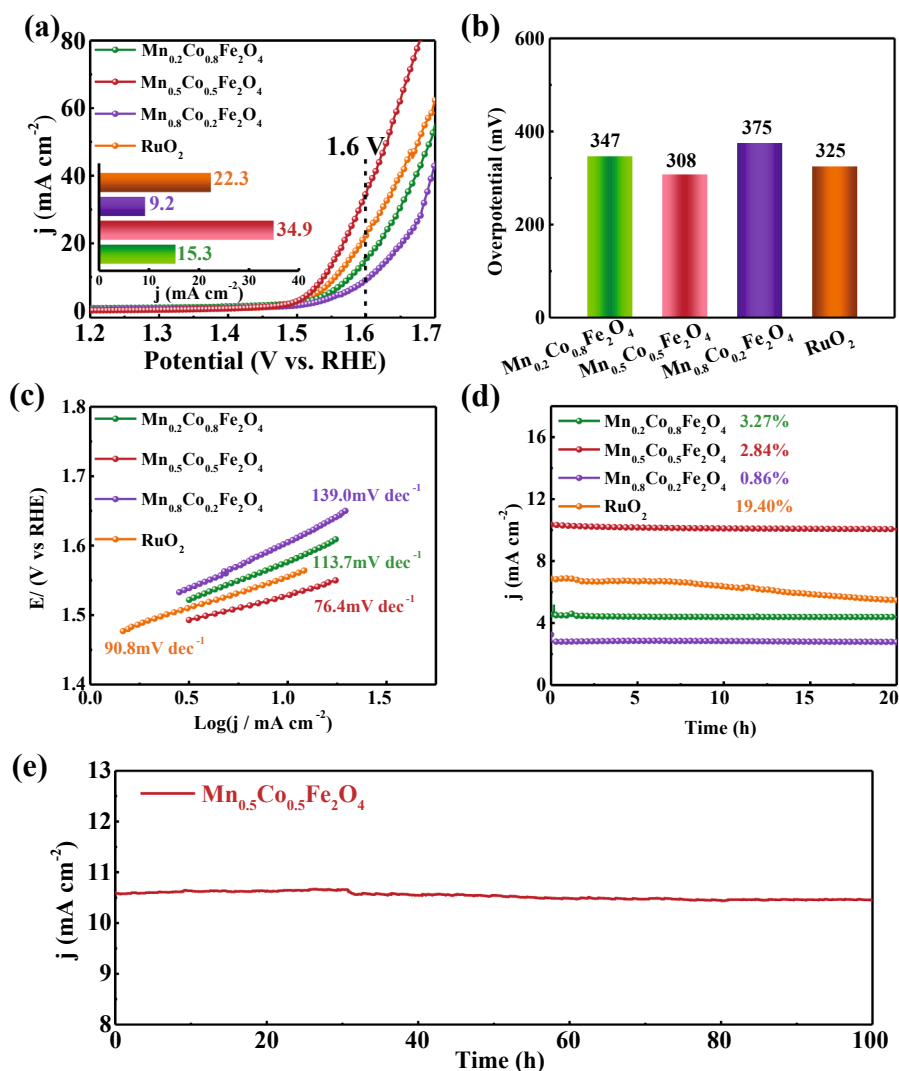

Fig. 3. OER performances of trimetallic cubic $Mn_xCo_{1-x}Fe_2O_4$ and commercial RuO_2 catalysts: (a) OER polarization curves in O_2-saturated 1.0 M KOH (Rotation rate: 1600 rpm, sweeping rate: 5 mV s^{-1}), inset shows the current densities at a chosen potential of 1.6 V; (b) Overpotentials at a current density of 10 mA cm^{-2}; (c) Tafel slopes derived from LSV curves in (a); (d) Chronoamperometric response of $Mn_{0.2}Co_{0.8}Fe_2O_4$, $Mn_{0.5}Co_{0.5}Fe_2O_4$, $Mn_{0.8}Co_{0.2}Fe_2O_4$ and RuO_2 at 1.54 V in O_2-saturated 1.0 M KOH; (e) Durability test for OER of $Mn_{0.5}Co_{0.5}Fe_2O_4$-14.5 nm within 100 h at 1.54 V in O_2-saturated 1.0 M KOH.

the same as the fresh sample, which implies the excellent durability for the OER. Oxygen reduction reaction (ORR) activities were also evaluated for those samples shown in **Figure S9**. Interestingly, the above $Mn_{0.5}Co_{0.5}Fe_2O_4$ also exhibited the best ORR performance among the $Mn_xCo_{1-x}Fe_2O_4$ catalysts, even higher than platinum catalyst (benchmark catalysts for oxygen reduction) in alkaline solution. Those results implied $Mn_{0.5}Co_{0.5}Fe_2O_4$ could be used as a promising bifunctional catalyst for both OER and ORR, which is necessary for regenerative fuel cell systems.

We further prepared another three $Mn_{0.5}Co_{0.5}Fe_2O_4$ catalysts with various particle sizes (6.3 nm, 14.5 nm, and 17.4 nm, **Figure S12**) to investigate the size effect on the OER performance. It is found that $Mn_{0.5}Co_{0.5}Fe_2O_4$-14.5 nm exhibited an even better OER activity (**Figure S13**) with an overpotential of 297 mV at a current density of 10 mA cm^{-2}, which is lower than most of the reported OER catalysts in **Table S2**. The durability test of the $Mn_{0.5}Co_{0.5}Fe_2O_4$-14.5 nm was evaluated by chronoamperometry as shown in Fig. 3e. Continuous evaluation of the OER for ca. 100 h on $Mn_{0.5}Co_{0.5}Fe_2O_4$-14.5 nm catalyst caused a tiny loss (only 1.13 %) in current density. The unprecedented durability for $Mn_{0.5}Co_{0.5}Fe_2O_4$-14.5 nm demonstrates its great application prospect in water splitting.

Two reference catalysts denoted as $Mn_{0.5}Co_{0.5}Fe_2O_4$-IM and $Mn_{0.5}Co_{0.5}Fe_2O_4$-DP were also prepared by incipient-wetness impregnation and deposition–precipitation, respectively. An irregular spherical-like morphology for $Mn_{0.5}Co_{0.5}Fe_2O_4$-DP with an average particle size of 15.9 ± 3.4 nm was observed in **Figure S8a**. However, it is very difficult to distinguish the spinel particles from the carbon support in $Mn_{0.5}Co_{0.5}Fe_2O_4$-IM catalyst (**Figure S8b**). As shown in **Figure S8c**, these two reference catalysts also showed the characteristic diffraction peaks of the inverse spinel structure (PDF#22–1086). Nevertheless, the relative diffraction peak intensity ratios of (400) to (311) facets (I_{400}/I_{311}) and (440) to (311) facets (I_{440}/I_{311}) in the reference samples were close to the standard PDF card of 22–1086, and they are much lower than those of cubic $Mn_{0.5}Co_{0.5}Fe_2O_4$ catalyst, indicating that only the cubic morphology could guarantee the preferred exposure of (400) and (440) facets. In **Figure S8d**, $Mn_{0.5}Co_{0.5}Fe_2O_4$-IM and $Mn_{0.5}Co_{0.5}Fe_2O_4$-DP showed an inferior OER performance, in which the overpotentials at a current density of 10 mA cm^{-2} are 357 mV and 354 mV, respectively, higher than that of $Mn_{0.5}Co_{0.5}Fe_2O_4$-cubic (308 mV) and RuO$_2$ (325 mV). As shown in **Figure S8e**, the Tafel slopes follow the order: $Mn_{0.5}Co_{0.5}Fe_2O_4$-IM (114.0 mV dec^{-1}) > $Mn_{0.5}Co_{0.5}Fe_2O_4$-DP (97.8 mV dec^{-1}) > RuO$_2$ (90.8 mV dec^{-1}) > $Mn_{0.5}Co_{0.5}Fe_2O_4$-Cubic (76.4 mV dec^{-1}). The inferior OER performance for the reference samples might be ascribed to their irregular morphologies and structures, which did not lead to the preferred exposure of the highly active (400) and (440) facets in the inverse spinel phase.

We also fabricated spherical $Mn_{0.5}Co_{0.5}Fe_2O_4$ inverse spinel samples as control sample (**Figure S10a**). The spherical $Mn_{0.5}Co_{0.5}Fe_2O_4$ have a similar mean particle size (11.5 ± 1.5 nm, **Figure S10c**) and metallic content (Fe: 67.3 atom%, Co: 16.7 atom %, Mn:16.0 atom%) to cubic $Mn_{0.5}Co_{0.5}Fe_2O_4$ nanoparticles (**Table S1**). As shown in **Figure S10b**, a distinct bright ring corresponding to the (311) plane emerged, which was not obvious in the SAED image of the cubic catalysts. In the XRD patterns in **Figure S10d**, the intensity of (311) plane was much higher in spherical particles, which has a much lower $I_{(400)}/I_{(311)}$ ratio of 0.77 than $Mn_{0.5}Co_{0.5}Fe_2O_4$ nanocubes ($I_{(400)}/I_{(311)} = 4.9$). As expected, the spherical $Mn_{0.5}Co_{0.5}Fe_2O_4$ showed a lower OER and ORR activity (**Figure S10e-S10f**), which might originate from the reduced fraction of active (400) and (440) planes. Similarly, we also compare the OER and ORR performance between spherical and cubic $CoFe_2O_4$ NPs (**Figure S11**), and found that cubic $CoFe_2O_4$ exhibited better OER and ORR performance than spherical one.

2.3. Oxygen evolution mechanism

To prove the mechanism of OER, we further performed in situ attenuated total reflection infrared (ATR-IR) spectroelectrochemical measurements to monitor the key reaction intermediate. As shown in Fig. 4a, the vibration bands at approximately 1,182 cm^{-1} are assigned to the characteristic vibration adsorption of the surface-adsorbed superoxide (OOH*) [45]. It is obvious that only the distinct vibration peak of *OOH at 1182 cm^{-1} was detected, and its intensity increases gradually with the improved potential, indicating the increase in the concentration of the adsorbed *OOH on the catalyst surface. This implies that the reaction pathway for OER in the Fe-based catalysts mainly follows the adsorbate evolution mechanism (AEM) rather than the lattice oxygen oxidation mechanism (LOM) (Fig. 4b), which rationalizes the excellent stability of $Mn_{0.5}Co_{0.5}Fe_2O_4$ during oxygen evolution process.

Mössbauer spectroscopy (MES) is one powerful tool for the identification of the Fe species in different phases [46]. There were two distinct coordination environments or locations for metal cation in the spinel structure, namely the tetrahedral site (A site) and octahedral site (B site) [47,48]. To clarify the coordination environment of Mn^{x+}, Co^{x+} and Fe^{x+} cations, the Mössbauer spectra were recorded at 77 K. As shown in Fig. 5, two sub-spectra could be deconvoluted for each sample, indicating there were two kinds of Fe species with different coordination environment, and the corresponding interaction parameters and the contents of each Fe species were listed in Table 1. In three tested samples, the sextet with parameters of isomer shift (*IS*) of 0.48–0.49 mm s^{-1}, quadrupole shift (*QS*) of 0.005–0.03 mm s^{-1}, hyperfine magnetic field (*H*) of 51.3–51.7 T could be attributed to Fe^{x+} cations in tetrahedral site, denoted as Fe(A); Another sextet with parameters of isomer shift (*IS*) of 0.42–0.43 mm s^{-1}, hyperfine magnetic field (*H*) of 48.6–49.3 T belonged to Fe^{x+} cations in octahedral site, denoted as Fe(B) [49–51].

In the Mössbauer spectra of Fe$_3$O$_4$/C in Fig. 5a, the molar ratio of Fe (A)/Fe(B) is close to 1/2, which is consistent with the nominal composition of the typical Fe$_3$O$_4$ spinel structure, and the corresponding model was shown in Fig. 5d. However, as shown in Fig. 5b, the ratio of Fe(A)/Fe(B) in CoFe$_2$O$_4$/C was close to 1/3, indicating that half of Co^{x+} cations were located in A site [Co(A)], while the others were in B site [Co(B)], and the structure was shown in Fig. 5e. In $Mn_{0.5}Co_{0.5}Fe_2O_4$/C, the ratio of Fe(A)/Fe(B) was similar to that in CoFe$_2$O$_4$/C, suggesting that half of $Co^{x+} + Mn^{x+}$ cations were located in A sites, and others were in B sites. According to the previous research on the inversion degree in $[M_{1-i}Fe_i]^A[M_iFe_{(2-i)}]^BO_4$ (M = Mn, Co, Ni), when M = Mn^{x+}, the inversion degree of i is ca. 0.20, while it is 0.68 when M is Co^{x+}, indicating that Mn^{x+} cations prefer to substituting the Fe^{x+} in A sites, while Co^{x+} cations tend to replace the Fe^{x+} in B sites [52]. Consequently, combining the Mössbauer spectra and the previous study, it could be concluded that most of Mn^{x+} (ca. 75%) in $Mn_{0.5}Co_{0.5}Fe_2O_4$/C located in A sites, and most of Co^{x+} (ca. 75%) substituted Fe^{x+} in B sites, the structure model of $Mn_{0.5}Co_{0.5}Fe_2O_4$/C was shown in Fig. 5f.

Finally, DFT calculations were employed to elucidate the fundamental reason for the excellent OER activity of $Mn_{0.5}Co_{0.5}Fe_2O_4$ spinel cubic catalyst. On the basis of the bulk structure of cubic Fe$_3$O$_4$, CoFe$_2$O$_4$, $Mn_{0.5}Co_{0.5}Fe_2O_4$ catalysts determined by Mössbauer spectroscopy, we further constructed the surface models of (400) and (311) facets and calculated the Gibbs free energies change (ΔG) of the OER. The optimized surface models of (400) and (311) facets were shown in Fig. 6a-6c and **Figure S14a-S14c**.

As shown in Fig. 6d, the potential-limiting step (PLS), during OER is the conversion of intermediate species OH* to O* process for $Mn_{0.5}Co_{0.5}Fe_2O_4$(400) and Fe$_3$O$_4$(400). The Gibbs free energy change (ΔG) value of $Mn_{0.5}Co_{0.5}Fe_2O_4$(400) (1.55 eV) is the smallest among all the catalysts, indicating that $Mn_{0.5}Co_{0.5}Fe_2O_4$(400) requires the smallest overpotential to drive water oxidation. And for CoFe$_2$O$_4$(400), Fe$_3$O$_4$ (311), CoFe$_2$O$_4$(311), $Mn_{0.5}Co_{0.5}Fe_2O_4$(311) (**Figure S14d**), the PLS is the intermediate species O* to OOH* process. The PLS ΔG value of CoFe$_2$O$_4$(400) (1.70 eV) is smaller than CoFe$_2$O$_4$(311) (1.76 eV), which indicates that the catalysts mainly exposed to (400) plane indeed require a lower overpotential to drive water oxidation than the catalyst mainly exposed to (311) plane. The ΔG value in the (311) facets follows
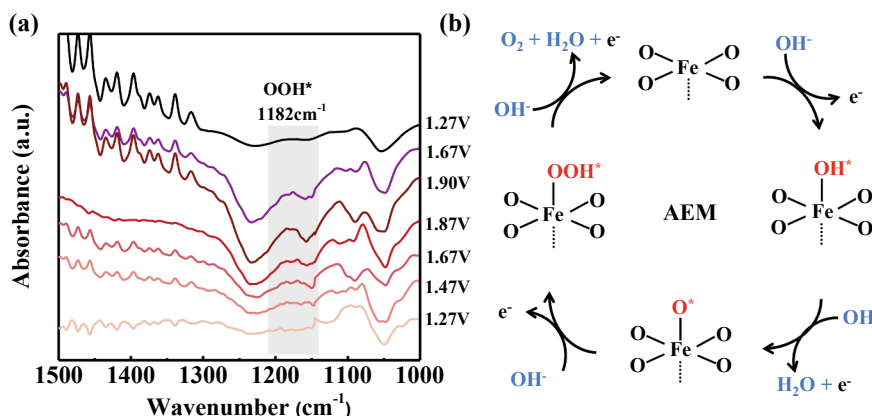
Fig. 4. (a) In situ ATR-IR spectra recorded with different potential steps. (b) The proposed adsorbate evolution mechanism (AEM).
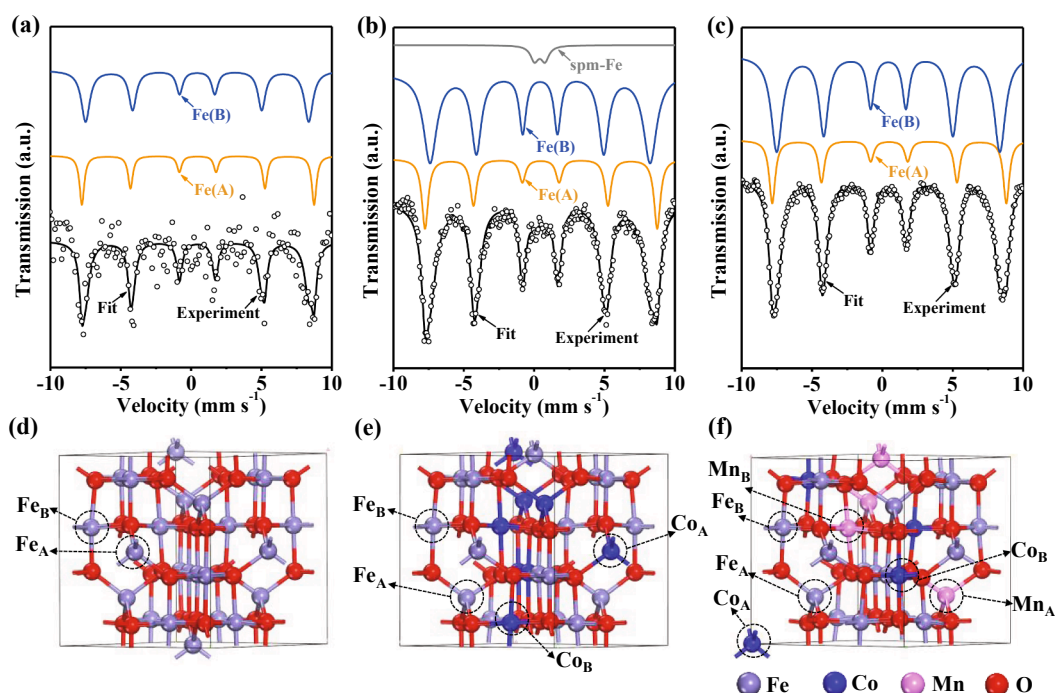

Fig. 5. ^{57}Fe Mössbauer spectroscopy of the supported catalysts determined at 77 K and the corresponding structural model of (a, d) Fe$_3$O$_4$/C; (b, e) CoFe$_2$O$_4$/C; (c, f) Mn$_{0.5}$Co$_{0.5}$Fe$_2$O$_4$/C.

Table 1
^{57}Fe Mössbauer parameters of Fe$_3$O$_4$/C, CoFe$_2$O$_4$/C and Mn$_{0.5}$Co$_{0.5}$Fe$_2$O$_4$/C catalysts determined at 77 K.

Catalysts	IS(mm s^{-1})[a]	QS(mm s^{-1})[b]	H(T)[c]	phase ascription	phase content (%)	Fe(A)/Fe(B) molar ratio
Fe$_3$O$_4$/C	0.48	0.02	51.3	Fe(A)	34.5	1/2
	0.43	–	49.3	Fe(B)	65.5	
CoFe$_2$O$_4$/C	0.48	0.03	51.3	Fe(A)	26.3	1/3
	0.42	–	48.6	Fe(B)	70.2	
	1.19	2.33	–	spm-Fe	3.6	
Mn$_{0.5}$Co$_{0.5}$Fe$_2$O$_4$/C	0.49	0.005	51.7	Fe(A)	26.1	1/3
	0.42	–	49.3	Fe(B)	73.9	

[a]: *IS*, isomer shift (relative to α-Fe); [b]: *QS*, quadrupole shift for sextet or quadruple splitting for doublet; [c]: *H*, hyperfine magnetic field.

the order of Mn$_{0.5}$Co$_{0.5}$Fe$_2$O$_4$(311) (1.62 eV) < CoFe$_2$O$_4$(311) (1.76 eV) < Fe$_3$O$_4$(311) (2.36 eV). Similarly, Yang et al. [53] also found that the rate-determining step (RDS) on the NiFe-LDH electrocatalysts is the conversion of O* to OOH*. As shown in **Figure S14**e, the average Bader charge of Fe atoms in CoFe$_2$O$_4$ is calculated to be +1.76 e, slightly higher than that the average Bader charge of Fe atoms in Fe$_3$O$_4$ (+1.72 e), which indicates that the incorporation of Co atoms into the spinel structure can increase the valent state of Fe atoms and the proper valance state of Fe exhibits a good OER activity. The above results indicate that the energy barrier of the PLS during the electrocatalytic process has
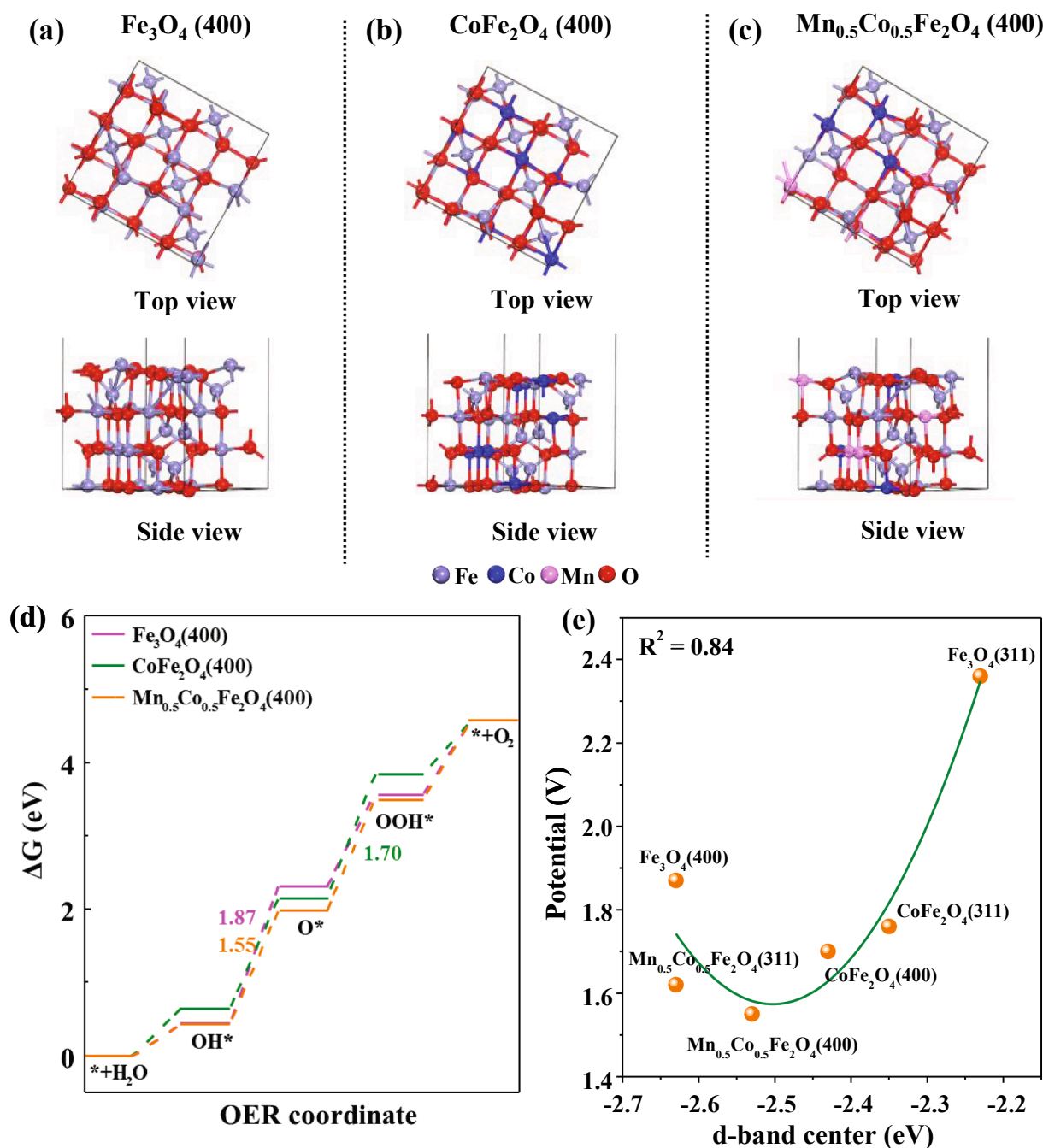
Fig. 6. The surface models of (a) $Fe_3O_4(400)$; (b) $CoFe_2O_4(400)$; (c) $Mn_{0.5}Co_{0.5}Fe_2O_4(400)$; (d) Gibbs free energy (ΔG) diagram for OER on $Fe_3O_4(400)$, $CoFe_2O_4(400)$, $Mn_{0.5}Co_{0.5}Fe_2O_4(400)$; (e) Relationships of the calculated d-band centers and limiting potential for oxygen evolution.

been reduced with the doping of Co and Mn, thereby improving the OER performance.

Previous researches have demonstrated that the water splitting activity is closely related to the electronic structure and the band position of the electrocatalysts. For example, Zhang et al. [54] reported that the incorporation of boron into $BiVO_4$ photoanodes could modulate the band position of $BiVO_4$ and enhance the charge separation of photo-hole pairs, thus facilitating the photoelectrochemical (PEC) water splitting. In addition, Hu et al. [55] found that the strong electronic interaction between Ni_2Fe_2N and Ni_3Fe enables low hydrogen adsorption energy and a shift in the d-orbital, which facilitated water dissociation and activation. As shown in Fig. 6e, an inverted volcano-shaped plot is presented between the potentials and calculated d-band center (E_d) energy level in these inverse spinel iron-based catalysts with various

composition and structure. The optimal E_d energy level is around -2.5 eV and the $Mn_{0.5}Co_{0.5}Fe_2O_4(400)$ is located closer to the inverted volcano bottom, which indicates that too low and too high E_d energy levels are both detrimental to the OER process. The Sabatier principle shows that the moderate adsorption and desorption energies of the reaction intermediates determine the catalytic efficiency [56–58]. Higher E_d energy levels, like Fe_3O_4, would cause strong bonding to the intermediates, which decelerate the desorption of the produced O_2, and eventually lead to the surface deactivation. Therefore, modulating morphology and doping appropriate Co and Mn to Fe_3O_4 inverse spinel oxides will endow a proper E_d energy level to balance the adsorption and desorption of intermediates.

3. Conclusions

In the present study, inverse spinel Fe-based nanoparticles were synthesized and well-tuned through a thermal decomposition process of the metal-oleate complex with oleic acid as the reducing agent in 1-octadecene solvent. Then Co and Mn were subsequently incorporated to enhance oxygen evolution performance. In an optimized sample, ternary $Mn_{0.5}Co_{0.5}Fe_2O_4$ nanocubes offer the best OER performance even higher than the benchmark RuO_2 catalyst. This originates from the optimized *d*-band center through the synergistic facet and composition effect, which results in a balanced adsorption strength of key reaction intermediate *OOH on catalyst surface during the oxygen evolution process.

Declaration of Competing Interest

The authors declare that they have no known competing financial interests or personal relationships that could have appeared to influence the work reported in this paper.

Acknowledgment

Appendix A. Supplementary data

Supplementary data to this article can be found online at https://doi.org/10.1016/j.cej.2021.134446.

References

[1] Y. Yang, H. Yao, Z. Yu, S.M. Islam, H. He, M. Yuan, Y. Yue, K. Xu, W. Hao, G. Sun, H. Li, S. Ma, P. Zapol, M.G. Kanatzidis, Hierarchical nanoassembly of $MoS_2/Co_9S_8/Ni_3S_2/Ni$ as a highly efficient electrocatalyst for overall water splitting in a wide pH range, J. Am. Chem. Soc. 141 (26) (2019) 10417–10430.

[2] Z. Morgan Chan, D.A. Kitchaev, J. Nelson Weker, C. Schnedermann, K. Lim, G. Ceder, W. Tumas, M.F. Toney, D.G. Nocera, Electrochemical trapping of metastable Mn^{3+} ions for activation of MnO_2 oxygen evolution catalysts, Proc. Natl. Acad. Sci. USA 115 (23) (2018) E5261–E5268.

[3] B. Rausch, M.D. Symes, G. Chisholm, L. Cronin, Decoupled catalytic hydrogen evolution from a molecular metal oxide redox mediator in water splitting, Science 345 (2014) 1326–1330.

[4] M. Gong, W. Zhou, M.C. Tsai, J. Zhou, M. Guan, M.C. Lin, B. Zhang, Y. Hu, D. Y. Wang, J. Yang, S.J. Pennycook, B.J. Hwang, H. Dai, Nanoscale nickel oxide/nickel heterostructures for active hydrogen evolution electrocatalysis, Nat. Commun. 5 (2014) 4695.

[5] N.T. Suen, S.F. Hung, Q. Quan, N. Zhang, Y.J. Xu, H.M. Chen, Electrocatalysis for the oxygen evolution reaction: Recent development and future perspectives, Chem. Soc. Rev. 46 (2017) 337.

[6] Z. Zhao, H. Liu, W. Gao, W. Xue, Z. Liu, J. Huang, X. Pan, Y.u. Huang, Surface-engineered PtNi-O nanostructure with record-high performance for electrocatalytic hydrogen evolution reaction, J. Am. Chem. Soc. 140 (29) (2018) 9046–9050.

[7] J. Xiong, J. Li, J. Shi, X. Zhang, N.-T. Suen, Z. Liu, Y. Huang, G. Xu, W. Cai, X. Lei, L. Feng, Z. Yang, L. Huang, H. Cheng, In situ engineering of double-phase interface in Mo/Mo_2C heteronanosheets for boosted hydrogen evolution reaction, ACS Energy Lett. 3 (2) (2018) 341–348.

[8] X. Tian, X. Zhao, Y.-Q. Su, L. Wang, H. Wang, D. Dang, B. Chi, H. Liu, E.J. M. Hensen, X.W.(. Lou, B.Y. Xia, Engineering bunched Pt-Ni alloy nanocages for efficient oxygen reduction in practical fuel cells, Science 366 (6467) (2019) 850–856.

[9] E. Detsi, J.B. Cook, B.K. Lesel, C.L. Turner, Y.-L. Liang, S. Robbennolt, S.H. Tolbert, Mesoporous $Ni_{60}Fe_{30}Mn_{10}$-alloy based metal/metal oxide composite thick films as highly active and robust oxygen evolution catalysts, Energy Environ. Sci. 9 (2) (2016) 540–549.

[10] L. Tian, X. Zhai, X. Wang, X. Pang, Z. Li, Morphology and phase transformation of α-MnO_2/MnOOH modulated by N-CDs for efficient electrocatalytic oxygen evolution reaction in alkaline medium, Electrochim. Acta 337 (2020) 135823.

[11] H. Yin, S. Zhao, K. Zhao, A. Muqsit, H. Tang, L. Chang, H. Zhao, Y. Gao, Z. Tang, Ultrathin platinum nanowires grown on single-layered nickel hydroxide with high hydrogen evolution activity, Nat. Commun. 6 (2015) 6430.

[12] A.T. Garcia-Esparza, T. Shinagawa, S. Ould-Chikh, M. Qureshi, X. Peng, N. Wei, D. H. Anjum, A. Clo, T.-C. Weng, D. Nordlund, D. Sokaras, J. Kubota, K. Domen, K. Takanabe, An oxygen-insensitive hydrogen evolution catalyst coated by a molybdenum-based layer for overall water splitting, Angew. Chem. Int. Ed. 56 (21) (2017) 5780–5784.

[13] M.S. Balogun, W. Qiu, Y. Huang, H. Yang, R. Xu, W. Zhao, G.R. Li, H. Ji, Y. Tong, Cost-effective alkaline water electrolysis based on nitrogen- and phosphorus-doped self-supportive electrocatalysts, Adv. Mater. 29 (2017) 1702095.

[14] L. Zhang, Q. Fan, K. Li, S. Zhang, X. Ma, First-row transition metal oxide oxygen evolution electrocatalysts: Regulation strategies and mechanistic understandings, Sustain, Energy Fuels 4 (11) (2020) 5417–5432.

[15] S. Zhang, Q. Fan, R. Xia, T. Meyer, CO_2 reduction: From homogeneous to heterogeneous electrocatalysis, Acc. Chem. Res. 53 (2020) 255–264.

[16] H. Liu, Y. Su, S. Kuang, E.J.M. Hensen, S. Zhang, X. Ma, Highly efficient CO_2 electrolysis within a wide operation window using octahedral tin oxide single crystals, J. Mater. Chem. A 9 (12) (2021) 7848–7856.

[17] L. Trotochaud, S.L. Young, J.K. Ranney, S.W. Boettcher, Nickel-iron oxyhydroxide oxygen-evolution electrocatalysts: the Role of intentional and incidental iron incorporation, J. Am. Chem. Soc. 136 (2014) 6744–6753.

[18] J.F.d.A. M Görlin, H. Schmies, D. Bernsmeier, S. Dresp, M. Gliech, Z. Jusys, P. Chernev, R. Kraehnert, H. Dau, Tracking catalyst redox states and reaction dynamics in Ni-Fe oxyhydroxide oxygen evolution reaction (OER) electrocatalysts: the Role of catalyst support and electrolyte pH, J. Am. Chem. Soc. 139 (2017) 2070-2082.

[19] M. Huynh, D.K. Bediako, D.G. Nocera, A functionally stable manganese oxide oxygen evolution catalyst in acid, J. Am. Chem. Soc. 136 (16) (2014) 6002–6010.

[20] M. Huynh, D.K. Bediako, Y.i. Liu, D.G. Nocera, Nucleation and growth mechanisms of an electrodeposited manganese oxide oxygen evolution catalyst, J. Phys. Chem. C 118 (30) (2014) 17142–17152.

[21] Y. Pi, Q.i. Shao, X. Zhu, X. Huang, Dynamic structure evolution of composition segregated iridium-nickel rhombic dodecahedra toward efficient oxygen evolution electrocatalysis, ACS Nano 12 (7) (2018) 7371–7379.

[22] Y. Pi, S. Qi, P. Wang, J. Guo, X. Huang, General formation of monodisperse IrM (M = Ni Co, Fe) bimetallic nanoclusters as bifunctional electrocatalysts for acidic overall water splitting, Adv. Funct. Mater. 27 (2017) 1700886.

[23] N. Zhang, Q.i. Shao, Y. Pi, J. Guo, X. Huang, Solvent-mediated shape tuning of well-defined rhodium nanocrystals for efficient electrochemical water splitting, Chem. Mater. 29 (11) (2017) 5009–5015.

[24] F.-D. Kong, S. Zhang, G.-P. Yin, J. Liu, Z.-Q. Xu, IrO_2-graphene hybrid as an active oxygen evolution catalyst for water electrolysis, Int. J. Hydrog. Energy 38 (22) (2013) 9217–9222.

[25] L. Tian, Z. Li, P. Wang, X. Zhai, X. Wang, T. Li, Carbon quantum dots for advanced electrocatalysis, J. Energy Chem. 55 (2021) 279–294.

[26] C. Hu, M. Li, J. Qiu, Y.-P. Sun, Design and fabrication of carbon dots for energy conversion and storage, Chem. Soc. Rev. 48 (8) (2019) 2315–2337.

[27] Y. Zhu, X. Ji, C. Pan, Q. Sun, C.E. Banks, A carbon quantum dot decorated RuO_2 network: Outstanding supercapacitances under ultrafast charge and discharge, Energy Environ. Sci. 6 (2013) 36653675.

[28] S. Sun, X. Jin, B. Cong, X. Zhou, W. Hong, G. Chen, Construction of porous nanoscale $NiO/NiCo_2O_4$ heterostructure for highly enhanced electrocatalytic oxygen evolution activity, J. Catal. 379 (2019) 1–9.

[29] G. Wu, W. Chen, X. Zheng, D. He, Y. Li, Hierarchical Fe-doped NiO_x nanotubes assembled from ultrathin nanosheets containing trivalent nckel for oxygen evolution reaction, Nano Energy 38 (2017) 167–174.

[30] X. Wang, L. Yu, B.Y. Guan, S. Song, X.W. Lou, Metal-organic framework hybrid-assisted formation of Co_3O_4 /Co-Fe oxide double-shelled nanoboxes for enhanced oxygen evolution, Adv. Mater. 30 (2018) 1801211.

[31] Y. Sun, H. Liao, J. Wang, B.o. Chen, S. Sun, S.J.H. Ong, S. Xi, C. Diao, Y. Du, J.-O. Wang, M.B.H. Breese, S. Li, H. Zhang, Z.J. Xu, Covalency competition dominates the water oxidation structure–activity relationship on spinel oxides, Nat. Catal. 3 (7) (2020) 554–563.

[32] Z.-F. Huang, J. Song, Y. Du, S. Xi, S. Dou, J.M.V. Nsanzimana, C. Wang, Z.J. Xu, X. Wang, Chemical and structural origin of lattice oxygen oxidation in Co–Zn oxyhydroxide oxygen evolution electrocatalysts, Nat. Energy 4 (4) (2019) 329–338.

[33] T. Wu, S. Sun, J. Song, S. Xi, Y. Du, B.o. Chen, W.A. Sasangka, H. Liao, C.L. Gan, G. G. Scherer, L. Zeng, H. Wang, H. Li, A. Grimaud, Z.J. Xu, Iron-facilitated dynamic active-site generation on spinel $CoAl_2O_4$ with self-termination of surface reconstruction for water oxidation, Nat. Catal. 2 (9) (2019) 763–772.

[34] T. Wang, J. Wang, Y. Sun, Y. Duan, S. Sun, X. Hu, S. Xi, Y. Du, C. Wang, Z.J. Xu, Origin of electronic structure dependent activity of spinel $ZnNi_xCo_{2-x}O_4$ oxides for complete methane oxidation, Appl. Catal. B-Environ. 256 (2019), 117844.

[35] Y. Duan, S. Sun, Y. Sun, S. Xi, X. Chi, Q. Zhang, X. Ren, J. Wang, S.J.H. Ong, Y. Du, L. Gu, A. Grimaud, Z.J. Xu, Mastering surface reconstruction of metastable spinel oxides for better water oxidation, Adv. Mater. 31 (2019) 1807898.

[36] Y. Zhou, S. Sun, J. Song, S. Xi, B. Chen, Y. Du, A.C. Fisher, F. Cheng, X. Wang, H. Zhang, Enlarged Co-O covalency in octahedral sites leading to highly efficient spinel oxides for oxygen evolution reaction, Adv. Mater. 30 (2018) 1802912.

[37] J. Lu, H. Wang, Y. Sun, X. Wang, X. Song, R. Wang, Charge state manipulation induced through cation intercalation into MnO_2 sheet arrays for efficient water splitting, Chem. Eng. J. 417 (2021), 127894.

[38] B. Zhang, L. Sun, Why nature chose the Mn_4CaO_5 cluster as water-splitting catalyst in photosystem II: a new hypothesis for the mechanism of O-O bond formation, Dalton Trans. 47 (2018) 14381–14387.

[39] I. Zaharieva, M.M. Najafpour, M. Wiechen, M. Haumann, P. Kurz, H. Dau, Synthetic manganese–calcium oxides mimic the water-oxidizing complex of photosynthesis functionally and structurally, Energy Environ. Sci. 4 (7) (2011) 2400, https://doi.org/10.1039/c0ee00815j.

[40] S. Park, Y.H. Lee, S. Choi, H. Seo, M.Y. Lee, M. Balamurugan, K.T. Nam, Manganese oxide-based heterogeneous electrocatalysts for water oxidation, Energy Environ. Sci. 13 (8) (2020) 2310–2340.

[41] M.V. Kovalenko, M.I. Bodnarchuk, R.T. Lechner, G. Hesser, F. Schäffler, W. Heiss, Fatty acid salts as stabilizers in size- and shape-controlled nanocrystal synthesis: the Case of inverse spinel iron oxide, J. Am. Chem. Soc. 129 (2007) 6352–6353.

[42] X.F. Lu, L.F. Gu, J.W. Wang, J.X. Wu, P.Q. Liao, G.R. Li, Bimetal-organic framework derived $CoFe_2O_4$ /C porous hybrid nanorod arrays as high-performance electrocatalysts for oxygen evolution reaction, Adv. Mater. 29 (2017) 1604437.

[43] Z. Zhao, W. Lu, R. Yang, H. Zhu, W. Dong, F. Sun, Z. Jiang, Y. Lyu, T. Liu, H. Du, Y. Ding, Insight into the formation of $Co@Co_2C$ catalysts for direct synthesis of higher alcohols and olefins from syngas, ACS Catal. 8 (1) (2018) 228–241.

[44] E. Beyreuther, S. Grafström, L.M. Eng, C. Thiele, K. Dörr, XPS investigation of Mn valence in lanthanum manganite thin films under variation of oxygen content, Phys. Rev. B 73 (2006), 155425.

[45] Y. Yao, S. Hu, W. Chen, Z.-Q. Huang, W. Wei, T. Yao, R. Liu, K. Zang, X. Wang, G. Wu, W. Yuan, T. Yuan, B. Zhu, W. Liu, Z. Li, D. He, Z. Xue, Y.u. Wang, X. Zheng, J. Dong, C.-R. Chang, Y. Chen, X. Hong, J. Luo, S. Wei, W.-X. Li, P. Strasser, Y. Wu, Y. Li, Engineering the electronic structure of single atom Ru sites via compressive strain boosts acidic water oxidation electrocatalysis, Nat. Catal. 2 (4) (2019) 304–313.

[46] X. Li, K. Zhu, J. Pang, M. Tian, J. Liu, A.I. Rykov, M. Zheng, X. Wang, X. Zhu, Y. Huang, B. Liu, J. Wang, W. Yang, T. Zhang, Unique role of Mössbauer spectroscopy in assessing structural features of heterogeneous catalysts, Appl. Catal. B-Environ. 224 (2018) 518–532.

[47] Q. Zhao, Z. Yan, C. Chen, J. Chen, Spinels: Controlled Preparation, Oxygen reduction/evolution reaction application, and beyond, Chem. Rev. 117 (2017) 10121–10211.

[48] X. Li, L. Yuan, J. Wang, L. Jiang, A.I. Rykov, D.L. Nagy, C. Bogdán, M.A. Ahmed, K. Zhu, G. Sun, W. Yang, A "copolymer-co-morphology" conception for shape-controlled synthesis of Prussian blue analogues and as-derived spinel oxides, Nanoscale 8 (4) (2016) 2333–2342.

[49] K.S. Al-Rashdi, H.M. Widatallah, F. Al Ma'Mari, O. Cespedes, M. Elzain, A. Al-Rawas, A. Gismelseed, A. Yousif, Structural and Mössbauer studies of nanocrystalline Mn^{2+}-doped Fe_3O_4 particles, Hyperfine Interact. 3 (2018) 239.

[50] K. Krieble, T. Schaeffer, J.A. Paulsen, A.P. Ring, C.C.H. Lo, J.E. Snyder, Mössbauer spectroscopy investigation of Mn-substituted Co-ferrite ($CoMn_xFe_{2−x}O_4$), J. Appl. Phys. 97 (2005) 10F101.

[51] D.H. Lee, H.S. Kim, C.H. Yo, K. Ahn, K.H. Kim, The magnetic properties and electrical conduction mechanism of $Co_{1−x}Mn_xFe_2O_4$ spinel, Mater. Chem. Phys. 57 (2) (1998) 169–172.

[52] D. Carta, M.F. Casula, A. Falqui, D. Loche, G. Mountjoy, C. Sangregorio, A. Corrias, A structural and magnetic investigation of the inversion degree in ferrite nanocrystals MFe_2O_4 (M=Mn Co, Ni), J. Phys. Chem. C 113 (20) (2009) 8606–8615.

[53] F. Yang, T. Xiong, P. Huang, S. Zhou, Q. Tan, H. Yang, Y. Huang, M.S. Balogun, Nanostructured transition metal compounds coated 3D porous core-shell carbon fiber as monolith water splitting electrocatalysts: A general strategy, Chem. Eng. J. 423 (2021) 130279.

[54] J. Zhang, Y. Huang, X. Lu, J. Yang, Y. Tong, Enhanced $BiVO_4$ photoanode photoelectrochemical performance via borate treatment and a $NiFeO_x$ cocatalyst, ACS Sustain. Chem. Eng. 9 (24) (2021) 8306–8314.

[55] Y. Hu, T. Xiong, M.S.J.T. Balogun, Y. Huang, D. Adekoya, S. Zhang, Y. Tong, Enhanced metallicity boosts hydrogen evolution capability of dual-bimetallic Ni–Fe nitride nanoparticles, Mater. Today Phys. 15 (2020), 100267.

[56] V.R. Stamenkovic, B.S. Mun, M. Arenz, K.J.J. Mayrhofer, C.A. Lucas, G. Wang, P. N. Ross, N.M. Markovic, Trends in electrocatalysis on extended and nanoscale Pt-bimetallic alloy surfaces, Nat. Mater. 6 (3) (2007) 241–247.

[57] J. Yan, L. Kong, Y. Ji, J. White, Y. Li, J. Zhang, P. An, S. Liu, S.-T. Lee, T. Ma, Single atom tungsten doped ultrathin α-$Ni(OH)_2$ for enhanced electrocatalytic water oxidation, Nat. Commun. 10 (2019) 1–10.

[58] S. Sun, X. Zhou, B. Cong, W. Hong, G. Chen, Tailoring the d-band centers endows $(Ni_xFe_{1−x})_2P$ nanosheets with efficient oxygen evolution catalysis, ACS Catal. 10 (16) (2020) 9086–9097.